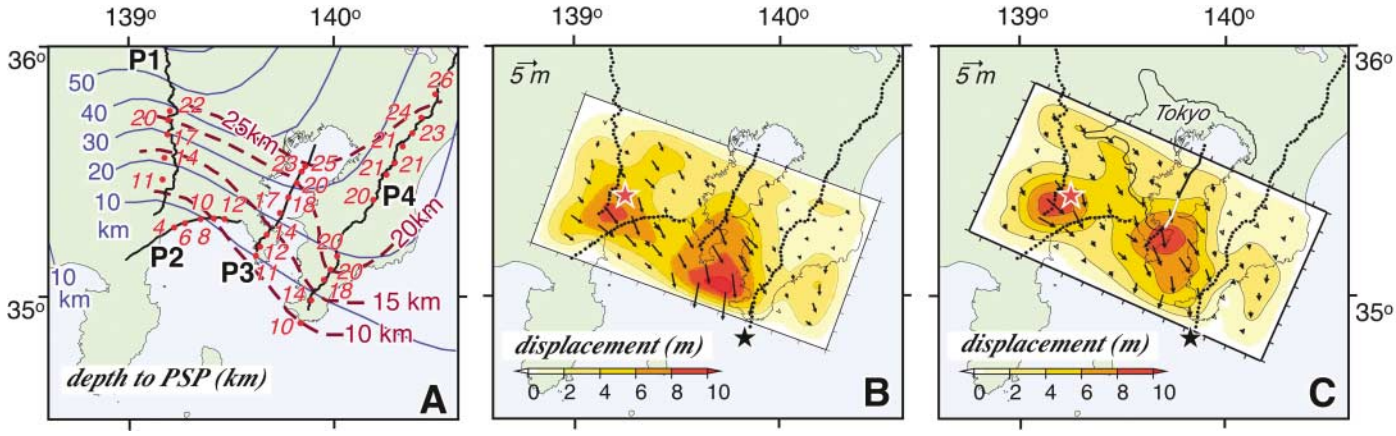

Fig. 3. PSP vertical and lateral characteristics derived from seismic profiles. (**A**) Depth to PSP in km. Blue contours are from a previously published study (*6*). Depths from seismic profiles are annotated (red) at marked locations (red dots); note substantial mismatch along P1 and northern P3. (**B**) 1923 Kanto earthquake finite-slip determination (*11*) based on previous fault model (*12*, *13*). Red zones of large displacement represent two asperity patches of 1923 Kanto earthquake rupture. (**C**) 1923 Kanto earthquake finite-slip determination recalculated with the use of our revised PSP geometry. Note the eastern red zone showing large coseismic slip is relocated northward toward the most densely populated area of greater Tokyo (solid outline). Stars are epicenters of 1703 Genroku (black) and 1923 Kanto earthquakes (red). Amplitude character color code along P3 defined in Fig. 2.

variable signal-to-noise recording conditions, particularly in the highly populated urban areas. The majority of P3 was acquired by using one marine seismic acquisition method and was amenable to relative amplitude seismic processing (*10*). The updip termination of UPSP reflection A in P3 (Fig. 2) correlates with the transition from low to high slip bounding the eastern asperity region (Fig. 3C). These revised geometries of the UPSP megathrust and its asperity regions as provided by our seismic profiles provide vertical and lateral constraints for improved estimations of seismic hazards within metropolitan Tokyo.

References and Notes

1. M. Takemura, *Great Kanto Earthquake* (Kajima, Tokyo, 2003).
2. The statistics were based on the 2003 annual report on the regional economy from the Cabinet Office of the Japanese government.
3. Y. Okada, *Earth Monthly* **34**, 94 (2001).
4. T. Seno *et al.*, *J. Geophys. Res.* **98**, 17941 (1993).
5. K. Kasahara, *Disaster Prev./Bosai* **35**, 33 (1985).
6. M. Ishida, *J. Geophys. Res.* **97**, 489 (1992).
7. S. Noguchi, *Bull. Earthquake Res. Inst. Univ. Tokyo* **73**, 73 (1998).
8. M. Matsubara *et al.*, *J. Geophys. Res.*, in preparation.
9. A. Taira *et al.*, in *The Evolution of the Pacific Ocean Margins*, Z. Ben-Abraham, Ed. (Oxford Univ. Press, New York, 1989), pp. 100.
10. See methods and data on *Science* Online.
11. R. Kobayashi, K. Koketsu, *Earth Planets Space* **57**, 261 (2005).
12. D. J. Wald, P. G. Somerville, *Bull. Seismol. Soc. Am.* **85**, 159 (1995).
13. M. Matsu'ura *et al.*, *J. Phys. Earth* **28**, 119 (1980).
14. T. Matsuzawa *et al.*, *Geophys. Res. Lett.* **29**, 11,1543 (2002).
15. Y. Yamanaka, M. Kikuchi, *J. Geophys. Res.* **109**, 1029/2003JB002683 (2004).
16. K. Koketsu, M. Kukuchi, *Science* **288**, 1237 (2000).
17. T. Furumura, K. Koketsu, *Pure Appl. Geophys.* **157**, 2047 (2000).
18. T. Sagiya, *Pure Appl. Geophys.* **161**, 2601 (2004).
19. S. Ozawa *et al.*, *Geophys. Res. Lett.* **30**, 1283 (2003).
20. S. Kodaira *et al.*, *J. Geophys. Res.* **105**, 5887 (2000).
21. S. Kodaira *et al.*, *Geophys. J. Int.* **149**, 815 (2002).
22. S. Kodaira *et al.*, *Science* **304**, 1295 (2004).
23. T. Hayakawa *et al.*, *Phys. Earth Planet. Inter.* **132**, 89 (2002).
24. A. Nakanishi *et al.*, *J. Geophys. Res.* **109**, 1029/2003JB002574 (2004).
25. M. Nedimovic *et al.*, *Nature* **424**, 416 (2003).
26. N. Bangs *et al.*, *J. Geophys. Res.* **104**, 20399 (1999).
27. T. Shipley *et al.*, *Geology* **22**, 411 (1994).
28. S. L. Bilek, T. Lay, *Science* **281**, 1175 (1998).
29. P. Wessel, W. H. F. Smith, *Eos* **72**, 445 (1991).

30. We thank K. Ito, K. Miller, J. Park, and F. Wu for discussions. Instruments used in the field program were provided by the seismic survey company JGI, Incorporated; ERI, the University of Tokyo; and the IRIS/PASSCAL instrument centers located at New Mexico Tech and University of Texas at El Paso (UTEP). We thank the JGI seismic crew and G. Kaip of UTEP for data acquisition. Figures were prepared with the use of the Generic Mapping Tool (*29*). This study was supported by the Special Project for Earthquake Disaster Mitigation in Urban Areas from the Ministry of Education, Culture, Sports, Science, and Technology of Japan.

Supporting Online Material

www.sciencemag.org/cgi/content/full/309/5733/462/DC1
Materials and Methods
Figs. S1 to S8

1 February 2005; accepted 27 May 2005
10.1126/science.1110489

Heat Flux Anomalies in Antarctica Revealed by Satellite Magnetic Data

Cathrine Fox Maule,[1]* Michael E. Purucker,[2] Nils Olsen,[1] Klaus Mosegaard[1]

The geothermal heat flux is an important factor in the dynamics of ice sheets; it affects the occurrence of subglacial lakes, the onset of ice streams, and mass losses from the ice sheet base. Because direct heat flux measurements in ice-covered regions are difficult to obtain, we developed a method that uses satellite magnetic data to estimate the heat flux underneath the Antarctic ice sheet. We found that the heat flux underneath the ice sheet varies from 40 to 185 megawatts per square meter and that areas of high heat flux coincide with known current volcanism and some areas known to have ice streams.

The geothermal heat flux depends on geologic conditions such as crustal heat production, mantle heat flux, and the tectonic history of the crust, which all vary spatially. Studies have shown that heat flux can vary much on scales less than 100 km (*1*, *2*). Underneath ice sheets, the geothermal heat flux influences the basal ice, which may cause varying amounts of basal melting in Greenland (*2*, *3*). Heat flux is thus an important boundary condition in ice sheet modeling. Little is known about the geologic setting of the crust underneath the

[1]Center for Planetary Science, Juliane Maries vej 30, 2100 Copenhagen Oe, Denmark. [2]Raytheon at Goddard Space Flight Center, NASA, Greenbelt, MD 20771, USA.

*To whom correspondence should be addressed. E-mail: foxmaule@gfy.ku.dk

Antarctic ice sheet from which the heat flux can be inferred, and direct measurements are hard to obtain because they require measurements at the bottom of ice boreholes reaching bedrock. So far, this has only been achieved at a few locations in Antarctica (*4*). The current available methods of (directly or indirectly) measuring the heat flux underneath the ice give only local results. Here, we present a method capable of providing a heat flux map covering Antarctica from satellite magnetic data. Using magnetic data to infer heat flux is possible because the magnetic properties of rocks are temperature dependent until they reach the Curie temperature (*5*). We use a magnetic field model based on satellite data to determine the depth to the Curie temperature, which is about 580°C for the low-Ti magnetite that is believed to be the dominant source of crustal magnetic anomalies (*6*). Combining this with a thermal model of the crust, we estimated the heat flux underneath the ice sheet.

On a global scale, Earth's magnetic field is dominated by contributions from the core, whereas only a few percent is of crustal origin. However, at wavelengths shorter than about 2600 km, the crustal part dominates the core field. The crustal field is caused by remanent magnetism and magnetism induced by the present core field. The latter depends on the magnetic susceptibility of the rocks, the ambient field strength, and the thickness of the magnetic crust, which is bounded above by bedrock surface and below by either Moho (*7*) or the Curie isotherm, whichever of the two is shallower. Thus, the magnetic crust can be thinner than the chemical crust in regions with high heat flux.

The measured magnetic field also includes time-varying contributions due to the interaction between the Earth's core field and the solar wind. The influence of the strong time-variable external field in polar regions is minimized by deriving spherical harmonic representations (field models) of the magnetic field with data from magnetically quiet times. Therefore, instead of using the satellite data directly, we based our analysis on the Magnetic Field Model 3 crustal field model (*8*), which is constructed from several years of data from the Challenging Minisatellite Payload and Oersted satellites and includes spherical harmonic terms up to degree and order 90. From this, we computed the vertical component at 300-km altitude (*9*). To remove the core field, we high-pass filtered by using only spherical harmonics above degree 14. However, this also eliminated the long-wavelength part of the crustal field. To isolate the induced part, we subtracted a model of the oceanic remanent field (*10*, *11*). Neither global nor regional models of remanent magnetism of continental areas exist, so we assumed that induced magnetism dominates here. The resulting induced field (Fig. 1A) is the data used in our modeling.

To infer the thickness of the magnetic crust from the induced field, we used the equivalent source magnetic dipole method (*12*), in which the crustal magnetization is represented by dipoles evenly distributed at the Earth's surface. We used 21,162 dipoles, each representing an area with a diameter of about 180 km. Because we used only the induced part of the field, the directions of the dipoles are given by the present core field; only their magnitudes (dipole moments) are determined from the magnetic data by forward modeling (*13*).

The average magnetization, inferred from the dipole moments, is proportional to the average magnetic susceptibility and the thickness of the magnetic crust. In general, the crustal field is stronger over the continents than over the oceans (*8*), and there is a relatively large difference between the continental (~40 km) and oceanic (~7 km) crustal thickness (*14*), whereas the difference in susceptibility between oceanic and continental rocks is not as large (*6*). It is therefore reasonable to assume that thickness variations dominate susceptibility variations. We used 0.035 (in the SI system, susceptibility has no unit) for the susceptibility of the continental crust and 0.040 for the oceanic crust (*15*). With this assumption, the magnetic crustal thickness can be determined from the magnetization. Only the short-wavelength variation of the magnetic crust is constrained by the magnetic field data (because of the high-pass filtering), so its long-wavelength part is taken from the 3SMAC crustal thickness model (*16*) (Fig. 1B), which is based on seismic and thermal data. Combining the long- and short-wavelength parts, we obtained the magnetic crustal thickness (Fig. 1C).

We found that the magnetic crustal thickness to some extent reflects the known crustal thickness difference between East and West Antarctica, with thicker crust in East than in West Antarctica (*16*, *17*). The magnetic crust is thicker in East Antarctica than in West Antarctica, and the thickest crust is in the central parts of East Antarctica. The area around Victoria Land, Oates Land, and George V Land in East Antarctica has a thin magnetic crust, as also found in a belt along the East-West Antarctica boundary and along the Siple Coast. Intermediate values of the magnetic crustal thickness are present in the coastal part of West Antarctica.

To estimate the geothermal heat flux, we constructed a thermal model for the continental crust, not including the ice [supporting online material (SOM) text]. We assumed that there was one-dimensional heat conduction, steady state, and constant thermal conductivity and that the lower boundary of the magnetic crust was the Curie isotherm. To account for radioactive heat production in the crust, we applied a model of exponentially decreasing heat production with depth (*18*), taking the heat production at the surface to be 2.5×10^{-6} W/m^3 and the scale depth to be 8 km [(*18*) and references therein]. The temperature difference over the magnetic crustal thickness is the difference between the Curie temperature and the temperature at the bedrock surface, which is close to 0°C underneath the ice sheet. With these boundary conditions, the heat conduction equation was solved to give the temperature-depth profile in the crust (SOM text). We obtained the heat flux at the bedrock surface from the temperature profile. We chose a thermal conductivity of 2.8 W/mK (*19*) and took the difference between the Curie temperature and the bedrock temperature to be 580 K. Choosing these values resulted in an average heat flux in Antarctica of 65 mW/m^2, which is the continental average (*20*). We validated our method using direct heat flux measurements in Australia; for error analysis we applied it to another geomagnetic field model, Comprehensive Model, Version 4 (*21*), and obtained similar results (<15 to 20% difference) to those presented here. Both indicate that magnetic anomalies are a robust proxy for geothermal heat flux (SOM text). Geothermal heat flux can vary on a scale of tens of kilometers as a result of local geologic settings (*1*, *2*). Satellite data limits our resolution to at least a few hundred kilometers, which causes a smoothing that should be kept in mind when comparing a heat flux map derived from satellite magnetic data with direct measurements.

The obtained heat flux map (Fig. 1D) reflects the variation in the magnetic crustal thickness. We found below average heat flux (50 to 60 mW/m^2) in the central part of East Antarctica and elevated heat flux along the East-West Antarctica boundary and around Siple Coast. Similarly high heat fluxes were found around Victoria Land, Oates Land, and George V Land. Our results are supported by geological evidence of high heat flux and may explain the occurrence of subglacial lakes and the Siple Coast ice streams. For example, around Victoria Land and in the coastal part of West Antarctica, areas of high heat flux coincide with current volcanic activity. At Siple Coast, where we found elevated heat flux, there are several ice streams, and it has previously been suggested that heat at the base of the ice could be one of the trigger mechanisms for their formation (*3*, *4*, *22*, *23*). Energy balance models (*24*) suggest that heat flux underneath one of the Siple Coast ice streams must exceed 80 mW/m^2 to maintain basal melting, which is the value we found for this area. Direct measurements at Siple Dome yield 69 mW/m^2 (*4*); the difference is within our error estimate (20 to 25 mW/m^2; SOM text). Subglacial lakes are widespread in Ant-

arctica (*25*). Studies on the thermal regime of the overlying ice sheet have shown that heat fluxes around 55 mW/m^2 are required to maintain the subglacial lakes in central parts of East Antarctica, whereas a substantially larger heat flux is necessary to maintain them in George V Land and Oates Land (*26*), in agreement with our results in these areas. In the Vostok area (78°S, 105°E), we found a heat flux of 54 mW/m^2, a value that exceeds the rate required to sustain a subglacial lake in this region [43 mW/m^2 in (*26*)]. On the basis of our results, one might speculate about volcanism in the area landward of Ronne Ice Shelf (*17*, *27*).

Errors in our estimate of geothermal heat flux (details in SOM text) beneath the Antarctic ice sheet arise through uncertainties in the magnetic field model (10 to 20 mW/m^2), unconsidered remanent magnetization (13 mW/m^2), our use of constant Curie and basal ice temperatures (5 mW/m^2), and lateral variations in thermal conductivity of the crustal rocks (10 mW/m^2). In addition, there are errors associated with uncertainties in the initial crustal model and lateral variations in magnetic susceptibility; although we are unable to quantify these contributions, we estimate that they are both less than 5 mW/m^2. The combined uncertainty of these independent, uncorrelated terms is 21 to 27 mW/m^2.

As an alternative to using satellite magnetic data, heat flux can be estimated from aeromagnetic data by, for example, power spectrum analysis (*28*). However, even with the creation of the Antarctic Digital Magnetic Anomaly Map (*29*), we believe that it currently would be difficult to make a Curie temperature depth map from aeromagnetic measurements covering Antarctica due to the sparsity of the data. The forte of power spectrum analysis of aeromagnetic data is that small-scale features can be resolved, but the method has difficulties at regional and global scales. Satellite data have the advantage of covering the entire Earth but can only see variations in excess of at least a few hundred kilometers (comparable to satellite altitude). Our results show that satellite magnetic data are a favorable way to estimate the regional scale of spatially varying

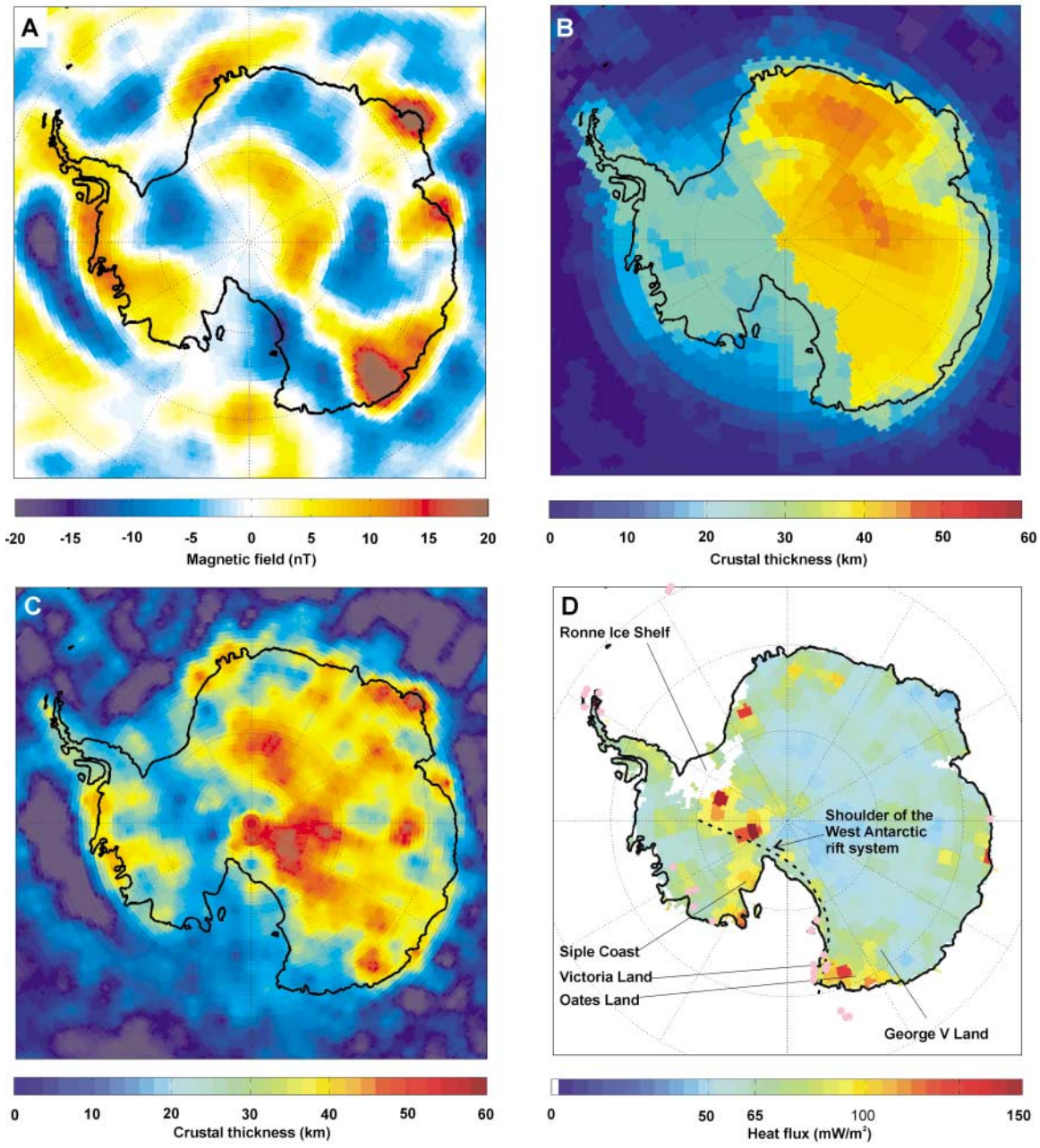

Fig. 1. (**A**) The radial component of the high-pass filtered observed magnetic field from MF3 at 300-km altitude, where a model of the remanent magnetism has been subtracted. Parallels are 10° apart, and meridians are 30° apart. (**B**) The initial model of crustal thickness from the 3SMAC model (*16*). (**C**) Obtained magnetic crustal thickness. The thickest magnetic crust is found in central parts of East Antarctica, and the thinnest crust is found around Victoria Land, Oates Land, and in the West Antarctic rift system. (**D**) Geothermal heat flux. The pink dots mark known volcanoes and coincide with areas of elevated heat flux, especially around Victoria Land. Areas of high heat flux are found close to the shoulder of the West Antarctic rift system (*17*). Because the heat flux model is valid only in continental areas, we have no results underneath Ronne Ice Shelf.

heat flux underneath large ice sheets. As the resolution of satellite magnetic field models improves in the future, this method will identify still finer features, and may eventually locate yet undiscovered volcanic areas (*27*) underneath the ice.

References and Notes

1. J.-O. Näslund, P. Jansson, J. L. Fastook, L. Andersson, J. Johnson, *Ann. Glaciol.*, in press.
2. D. Dahl-Jensen, N. Gundestrup, S. P. Gogineni, H. Miller, *Ann. Glaciol.* **37**, 207 (2003).
3. M. Fahnestock, W. Abdalati, I. Joughin, J. Brozena, P. Gogineni, *Science* **294**, 2338 (2001).
4. H. Engelhardt, *J. Glaciol.* **50**, 251 (2004).
5. The Curie temperature is the temperature above which materials lose their ability to sustain a (remanent or induced) magnetic field.
6. R. A. Langel, W. J. Hinze, *The Magnetic Field of the Earth's Lithosphere* (Cambridge Univ. Press, Cambridge, 1998).
7. Moho is the base of the chemical crust and is defined by seismic properties.
8. S. Maus, www.gfz-potsdam.de/pb2/pb23/SatMag/litmod3.html.
9. Although it is possible to calculate the field at any altitude from a spherical harmonic representation, downward continuation from satellite altitudes (400 to 800 km) amplifies shorter wavelengths. To avoid fitting artificial signatures due to amplified noise, we found that 300-km altitude was suitable for our parameter spacing.
10. J. Dyment, J. Arkani-Hamed, *J. Geophys. Res.* **103**, 15,423 (1998).
11. M. E. Purucker, J. Dyment, *Geophys. Res. Lett.* **27**, 2765 (2000).
12. J. Dyment, J. Arkani-Hamed, *Geophys. Res. Lett.* **25**, 2003 (1998).
13. C. Fox Maule, M. E. Purucker, N. Olsen, in *Earth Observation with CHAMP*, C. Reigber, H. Lühr, P. Schwintzer, J. Wickert, Eds. (Springer, Heidelberg, Germany, 2005).
14. W. Lowrie, *Fundamentals of Geophysics* (Cambridge Univ. Press, Cambridge, 1997).
15. M. E. Purucker, B. Langlais, N. Olsen, G. Hulot, M. Mandea, *Geophys. Res. Lett.* **29**, 10.1029/2001GL013645 (2002).
16. H.-C. Nataf, Y. Ricard, *Phys. Earth Planet. Inter.* **95**, 101 (1996).
17. J. C. Behrendt, *Global Planet. Change* **23**, 25 (1999).
18. M. Sandiford, S. McLaren, *Earth Planet. Sci. Lett.* **204**, 133 (2002).
19. G. R. Beardsmore, J. P. Cull, *Crustal Heat Flow* (Cambridge Univ. Press, Cambridge, 2001).
20. H. N. Pollack, S. J. Hurter, J. R. Johnson, *Rev. Geophys* **31**, 267 (1993).
21. T. J. Sabaka, N. Olsen, M. E. Purucker, *Geophys. J. Int.* **159**, 521 (2004).
22. D. D. Blankenship *et al.*, *Nature* **361**, 526 (1993).
23. M. R. Bennett, *Earth Sci. Rev.* **61**, 309 (2003).
24. C. F. Raymond, *J. Glaciol.* **46**, 665 (2000).
25. M. J. Siegert, *Earth Sci. Rev.* **50**, 29 (2000).
26. M. J. Siegert, J. A. Dowdeswell, *J. Glaciol* **42**, 501 (1996).
27. J. P. Winberry, S. Anandakrishnan, *Geophys. Res. Lett.* **30**, 10.1029/2003GL018001 (2003).
28. A. Stampolidis, G. N. Tsokas, *Pure Appl. Geophys.* **159**, 2659 (2002).
29. A. Golynsky *et al.*, *IX ISAES Proc.* (Springer, Heidelberg, in press).

30. We thank D. Dahl-Jensen and C. Hvidberg for comments on ice sheet stability and ice streams, and S. Maus for making MF3 available to us.

Supporting Online Material
www.sciencemag.org/cgi/content/full/1106888/DC1
SOM Text
Figs. S1 and S2
References

28 October 2004; accepted 1 June 2005
Published online 9 June 2005;
10.1126/science.1106888
Include this information when citing this paper.

RNA Polymerase II Is Required for RNAi-Dependent Heterochromatin Assembly

Hiroaki Kato,[1] Derek B. Goto,[2] Robert A. Martienssen,[2] Takeshi Urano,[3] Koichi Furukawa,[3] Yota Murakami[1]*

In *Schizosaccharomyces pombe*, the RNA interference (RNAi) machinery converts pericentromeric transcripts into small interfering RNAs (siRNAs) and is required for the assembly of pericentromeric heterochromatin. Here we describe a mutation in the second largest subunit of RNA polymerase II (RNAPII). Both wild-type and mutant RNAPII localized to the pericentromere. However, the mutation resulted in the loss of heterochromatic histone modifications and in the accumulation of pericentromeric transcripts, accompanied by the loss of siRNAs. This phenotype resembles mutants in RNAi and suggests that RNAPII couples pericentromeric transcription with siRNA processing and heterochromatin assembly.

Heterochromatin contributes to epigenetic regulation by inhibiting gene expression in specific chromosomal domains. RNAi-related factors play essential roles in heterochromatin formation (*1*–*3*). In the fission yeast *Schizosaccharomyces pombe*, transcripts from pericentromeric repeats generate siRNAs, which are responsible, at least in part, for targeting the RNAi-induced transcriptional silencing (RITS) complex. This targeting promotes histone H3–lysine 9 (H3-K9) dimethylation by the Clr4/Rik1 histone methyltransferase complex (*4*) that is required for the localization of Swi6, a heterochromatin protein 1 (HP1) homolog. These factors are conserved in higher eukaryotes, suggesting that siRNA-directed heterochromatin formation is an evolutionarily conserved mechanism (*5*). To further understand the mechanism of pericentromeric heterochromatin formation, we screened for mutations in fission yeast that affect pericentromeric heterochromatin. This led to the discovery of a previously undescribed mutation denoted as *m203* (*6*).

The *m203* mutation resulted in derepression of *ura4*$^+$ marker genes integrated into the outermost (*otr*) or innermost (*imr*) pericentromeric repeats of chromosome 1 (*otr1R::ura4*$^+$ and *imr1L::ura4*$^+$, respectively) (fig. S1). The extent of derepression was similar to that observed in RNAi-related ribonuclease III (RNase III) Dicer or histone H3K9 methyltransferase mutants (Δ*dcr1* and Δ*clr4*, respectively) (Fig. 1A). Like Δ*dcr1*, but unlike Δ*clr4*, the *m203* mutation did not affect silencing of the *ura4*$^+$ marker gene at the *mat* locus (*kint2::ura4*$^+$) (Fig. 1A). Thus, like mutants in RNAi, the *m203* mutation specifically disturbs pericentromeric silencing. We next demonstrated that the *m203* mutation alters the heterochromatic structure of the *ura4*$^+$ gene inserted at the *otr* locus by chromatin immunoprecipitation (ChIP) with antibodies specific for several modified histones or Swi6 (Fig. 1B). The *m203* mutation reduced H3-K9 methylation and Swi6 localization while increasing H3-K9 acetylation and H3-K4 methylation, both of which are euchromatic histone modifications (Fig. 1B). These changes are similar to those observed in Δ*dcr1* and Δ*clr4* mutants (Fig. 1B) (*3*, *7*). In addition, the *m203* mutation, like Δ*dcr1* and Δ*clr4*, impaired chromosome segregation (supporting online text, fig. S2), probably because of a defect in pericentromeric heterochromatin that resulted in improper sister chromatid cohesion (*8*, *9*).

Using genetic mapping and DNA sequencing (*6*), we identified an A-to-T base substitution within the *rpb2* gene, which encodes the second largest subunit (Rpb2) of RNA polymerase II (RNAPII), as the *m203* mutation. This allele is denoted as *rpb2-m203*, and the base substitution caused an alteration of asparagine-44 (Asn^{44}) to tyrosine (Tyr) (Fig. 2).

The *rpb2*$^+$ gene is essential for viability (*10*), but the *rpb2-m203* mutation did not impair growth at temperatures ranging from 23° to 36°C, indicating that its essential function was not affected by the mutation (fig. S4). In support of this, levels of constitutively expressed *act1* transcripts were not down-

[1]Department of Viral Oncology, Institute for Virus Research, Kyoto University, Kyoto 606–8507, Japan. [2]Cold Spring Harbor Laboratory, Cold Spring Harbor, NY 11724, USA. [3]Department of Biochemistry II, Nagoya University Graduate School of Medicine, Nagoya 466–8550, Japan.

*To whom correspondence should be addressed. Department of Viral Oncology, Institute for Virus Research, Kyoto University, Shogoinkawahara-cho, Sakyo-ku, Kyoto, Kyoto 606-8507, Japan. E-mail: yota@virus.kyoto-u.ac.jp

Heat Flux Anomalies in Antarctica Revealed by Satellite Magnetic Data

Cathrine Fox Maule, Michael E. Purucker, Nils Olsen and Klaus Mosegaard

Science **309** (5733), 464-467.
DOI: 10.1126/science.1106888originally published online June 9, 2005